



# Combination of ultrafast dye-sensitized-assisted electron transfer process and novel Z-scheme system: AgBr nanoparticles interspersed MoO<sub>3</sub> nanobelts for enhancing photocatalytic performance of RhB

Bing Feng<sup>a</sup>, Zhengying Wu<sup>b</sup>, Jinsong Liu<sup>a,c,\*</sup>, Kongjun Zhu<sup>c,\*\*</sup>, Ziquan Li<sup>a</sup>, Xin Jin<sup>d</sup>, Yindi Hou<sup>a</sup>, Qingsyang Xi<sup>a</sup>, Mengqi Cong<sup>a</sup>, Pengcheng Liu<sup>c</sup>, Qilin Gu<sup>c</sup>

<sup>a</sup> College of Materials Science and Technology, Nanjing University of Aeronautics and Astronautics, Nanjing, Jiangsu 211100, China

<sup>b</sup> Jiangsu Key Laboratory for Environment Functional Materials, School of Chemistry, Biology and Material Engineering, Suzhou University of Science and Technology, Suzhou 215009, China

<sup>c</sup> State Key Laboratory of Mechanics and Control of Mechanical Structures, Nanjing University of Aeronautics and Astronautics, Nanjing, Jiangsu 210016, China

<sup>d</sup> CAS Key Laboratory of Materials for Energy Conversion, Department of Materials Science and Engineering, University of Science and Technology of China, Hefei 230026, China

## ARTICLE INFO

### Article history:

Received 4 November 2016

Received in revised form 8 January 2017

Accepted 11 January 2017

Available online 16 January 2017

### Keywords:

Z-scheme photocatalyst

AgBr/MoO<sub>3</sub>

Dye-sensitized-assisted electron transfer

Theoretical calculations

Degradation mechanism

## ABSTRACT

Inspired by the natural photosynthesis in green plants, artificial heterogeneous Z-scheme photocatalytic systems are widely used to settle environmental concerns and energy crises, and their excellent characteristics come from long-term stability, wide absorption range, high charge-separation efficiency, and strong redox ability. However, the contribution of the surface-adsorbed dyes antenna molecule is seldom considered in the process of Z-scheme photocatalysis. In this study, we construct AgBr quantum dots decorated MoO<sub>3</sub> nanobelts as a novel Z-scheme photocatalyst by an oriented diffusing and charge induced deposition. For the first time, we find the synergistic effect caused by the suitable energy band match among RhB dyes, AgBr nanoparticles, and MoO<sub>3</sub> nanobelts, leading to the ultrafast dye-sensitized-assisted electron transfer process. This is responsible for excellent photocatalytic activities of the achieved AgBr/MoO<sub>3</sub> monolithic catalyst for degrading RhB under visible light irradiation. Simultaneously, changing of the band gaps and detailed mechanism for high efficiency degradation is analyzed and explored by theoretical calculations and designing further experiments. It is proposed that ultrafast degradation of the RhB on the AgBr/MoO<sub>3</sub> nanocomposites is due to both the photocatalytic process and the dye sensitization; the superoxide radical  $\bullet\text{O}_2^-$ , which is produced by accumulated dye-sensitization-induced abundant electrons with powerful potential in the CB of AgBr accompanying by quick combination of electrons in the CB of MoO<sub>3</sub> with photogenerated holes in the VB of AgBr, is a dominant reactive species for the degradation of RhB under visible light irradiation.

© 2017 Elsevier B.V. All rights reserved.

## 1. Introduction

As an advanced oxidation process over the surface of a semiconductor-based photocatalyst, visible-light-driven photocatalysis can be used to deal with growing environmental pollution through the conversion of solar energy to decompose organic pollutants into CO<sub>2</sub> and other small molecular substances [1–3].

Obviously, for the convenient and cost-effective single-component photocatalyst, the photoinduced carriers of the narrow band gap single-component photocatalyst can easily recombine while it is difficult to generate photogenerated electrons and holes for wide band gap single-component photocatalyst, which directly caused the poor quantum efficiency and low photocatalytic performance [4]. As one of many methods developed to enhance the photocatalytic performance [5–7], heterojunction structure created between the connected p- and n-type semiconductors recently attracts the most interest of researchers [8–10]. Driven by the inner-electric field, the photoinduced carriers are efficiently separated and transferred which inhibits their recombination. Unfortunately, both the oxidizability and reducibility of corresponding h<sup>+</sup> and

\* Corresponding author at: College of Materials Science and Technology, Nanjing University of Aeronautics and Astronautics, Nanjing, Jiangsu 211100, China.

\*\* Corresponding author.

E-mail addresses: [jsliu@nuaa.edu.cn](mailto:jsliu@nuaa.edu.cn) (J. Liu), [kjzhu@nuaa.edu.cn](mailto:kjzhu@nuaa.edu.cn) (K. Zhu).

$e^-$  usually become weakened after charge transfer, consequently decreasing the photocatalytic efficiency. Inspired by the natural photosynthesis in green plants, the construction of artificial heterogeneous Z-scheme photocatalytic system is an ideal and effective means because it possesses the high charge-separation efficiency and strong redox ability at the same time. According to the previous reports, most of the synthesized Z-scheme photocatalytic systems usually contained noble metal (Ag, Au, Pt, Ru) or redox pair ( $\text{IO}_3^-/\text{I}^-$ ,  $\text{Fe}^{3+}/\text{Fe}^{2+}$ ), which will restrict their practical application [11–15]. Actually, different types of carriers (such as electrons or holes) always do not play the same roles for the photocatalytic process, and it is more important to activate the redox ability of specific carriers by appropriate methods. Therefore, it is significant to construct a new Z-scheme system with two appropriate photocatalysts based on the specific reactive species.

Among the family of semiconductor materials,  $\text{MoO}_3$  is one of the most noticeable star materials due to its chemical stability, non-toxicity and abundant in source, and has been widely applied in many fields including wastewater treatment [16], capacitors [17], heterojunction photovoltaics [18], cathode material for lithium [19] and sodium-ion batteries and electrocatalytic materials [20]. Despite low quantum yield and large band gap (2.7–3.2 eV) of  $\text{MoO}_3$  layered material were not conducive to the photocatalytic performance, but its excellent dye adsorption capacity (as showed in SI) is significant for photocatalysis process [21]. To availablely degrade the adsorbed pollutants,  $\text{MoO}_3$  must be collaborated with other applicable semiconductor or element to form heterojunctions or compounds. Belt-like  $\alpha\text{-MoO}_3$ , which possesses rectangular cross section and uniform width or thickness, has attracted particular interest due to its anisotropic structure, fast charge transfer dynamics, larger surface to volume ratio with specifically exposed crystal facets [6]. Up to now, a series of products have been studied, such as  $\alpha\text{-MoO}_3@\text{MoS}_2$  [22],  $\text{TiO}_2/\text{MoO}_3$  [23],  $g\text{-C}_3\text{N}_4/\text{MoO}_3$  [24],  $\text{Bi}_2\text{Mo}_3\text{O}_{12}/\text{MoO}_3$  heterostructures [16] and so on. Even so, to further shorten degradation period and improve degradation efficiency is still a challenge. Moreover, there is no report on  $\text{MoO}_3$ -based Z-scheme heterojunctions so far according to our knowledge. Therefore, it is necessary to construct the  $\text{MoO}_3$ -based direct solid-state Z-scheme system with a visible-light-driven semiconductor photocatalyst for enhancing the photocatalytic efficiency.

In this study, we constructed AgBr quantum dots decorated  $\text{MoO}_3$  nanobelts to combine superior azo-dyes adsorptive capacity of  $\text{MoO}_3$  nanobelts with the high visible light absorption of AgBr, and the composite prospectively displayed excellent photocatalytic activities for degrading RhB under visible light irradiation. Subsequently, the changing of the band gaps was analyzed by theoretical calculations, and the reason for high efficiency degradation was investigated by designing further experiments including trapping reactive species and degrading visible light-insensitive thiophene. Finally, the probable mechanism for the photocatalysis process was proposed and discussed in detailed. This work provides a novel way for designing photocatalytic system consists of a substrate material with high pollutant adsorption ability and an antenna material with high visible light visible-light response.

## 2. Experimental section

### 2.1. Materials

All reagents were analytical grade and used without further purification. Molybdenum powder (Mo, AR), Rhodamine B ( $\text{C}_{28}\text{H}_{31}\text{ClN}_2\text{O}_3$ , AR) and barium sulfate ( $\text{BaSO}_4$ , AR) were used as reagents and supplied by Aladdin. Silver nitrate ( $\text{AgNO}_3$ , AR), Absolute ethyl alcohol ( $\text{C}_2\text{H}_5\text{OH}$ , AR), hydrogen peroxide ( $\text{H}_2\text{O}_2$ , 30%wt), sodium bromide (NaBr, AR), isoctane ( $(\text{CH}_3)_2\text{CHCH}_2\text{C}(\text{CH}_3)_3$ , AR),

thiophene ( $\text{C}_4\text{H}_4\text{S}$ , AR) were purchased from Sinopharm Chemical Reagent (Shanghai, China). Deionized water was produced using a Direct-Q Millipore filtration system having resistivity = 18.2 M $\Omega$  cm.

### 2.2. Preparation

$\text{MoO}_3$  nanobelts were prepared by a modified hydrothermal method [25]. In a typical procedure, metallic molybdenum powder (0.72 g) was dissolved into deionized water (35 mL) by shaking and then ultrasonic treatment for 10 min, respectively. Next, 30%wt  $\text{H}_2\text{O}_2$  (8 mL) was slowly added dropwise and the mixture was stirred for 20 min. The color of the mixed suspension changed from grey to dark blue as reaction time increased, and finally turned into a clarified yellow solution. Afterwards, the yellow solution was then placed in a 60 mL autoclave with a Teflon liner, the autoclave was maintained at 180 °C for 12 h and air-cooled to room temperature. The precipitates were collected and washed with deionized water and anhydrous alcohol three times and then dried in a vacuum at 80 °C for 12 h. The color of the resulting products was grey white. AgBr/ $\text{MoO}_3$  composites were prepared by a simple deposition-precipitation method at room temperature. The as-prepared  $\text{MoO}_3$  (0.5 g) was added to absolute ethyl alcohol (80 mL) with shaking vigorously for 5 min, and then NaBr (0.119 g) in distilled water (10 mL) was added and the mixture was sonicated for 10 min. Then,  $\text{AgNO}_3$  (0.1 mol L<sup>-1</sup>, 12 mL) was slowly added dropwise into the suspension. The resulting suspensions were stirred at room temperature for 12 h. Finally, the product was filtered, washed with water and absolute ethyl alcohol, then dried in air circulation oven at 70 °C. For comparison, the pure AgBr sample was prepared without adding  $\text{MoO}_3$ .

### 2.3. Sample characterization

Crystal structures of the products were identified by X-ray diffractometer (XRD, Rigaku D-max- $\gamma$ A XRD with Cu K $\alpha$  radiation,  $\lambda = 1.54178 \text{ \AA}$ ) operating at 40 KV and 40 mA. Scan range 2 $\theta$  was 10–80° and scan speed was 2° min<sup>-1</sup>. Morphologies and composition of the samples were characterized using an S-4800 (SEM, Hitachi, Japan) field emission scanning electron microscopy, which was equipped with an energy-dispersive spectrometer (EDS). Transmission electron microscopy (TEM) images were obtained using a Tecnai G2 F30 S-Twin instrument at an accelerating voltage of 200 kV. UV-vis absorption spectra were measured on JASCO V-670 UV-vis-NIR spectrophotometer via diffuse reflectance mode, and a pure  $\text{BaSO}_4$  pellet was employed as a reference. Photoluminescence (PL) spectra for solid samples were investigated on an Edinburgh FL/FS900 spectrophotometer with an excitation wavelength of 325 nm. Nitrogen adsorption and desorption isotherms were measured on an ASAP-2460 instrument. Electrochemical impedance spectroscopy (EIS) measurements: slurry of as-prepared powder (80 wt%), polyvinylidene fluoride (PVDF) binder (10 wt%), and a cetylene black (10 wt%) dissolved in *N*-methylpyrrolidone (NMP), and then pasted on Al current collector using a medical blade technique. Then, the electrode was dried under vacuum at 110 °C for 12 h and punched into 12 mm diameter disc. The total mass loading on the current collector was about 2 mg. CR2016 coin cells were assembled in an argon-filled glove box with the as-as-prepared powder cathode, with the lithium metal as anode and polypropylene film as separator. Electrolytes were 1 mol L<sup>-1</sup> LiPF<sub>6</sub> in a volumetric ratio with 1:1 mixture of ethylene carbonate (EC) and dimethyl carbonate (DMC). Electrochemical impedance spectrum (EIS) was measured by using a CHI 660E electrochemical workstation in the frequency range 10<sup>-2</sup>–10<sup>6</sup> Hz. Photoelectrochemical measurement of photocatalysts: photoelectrochemical proper-

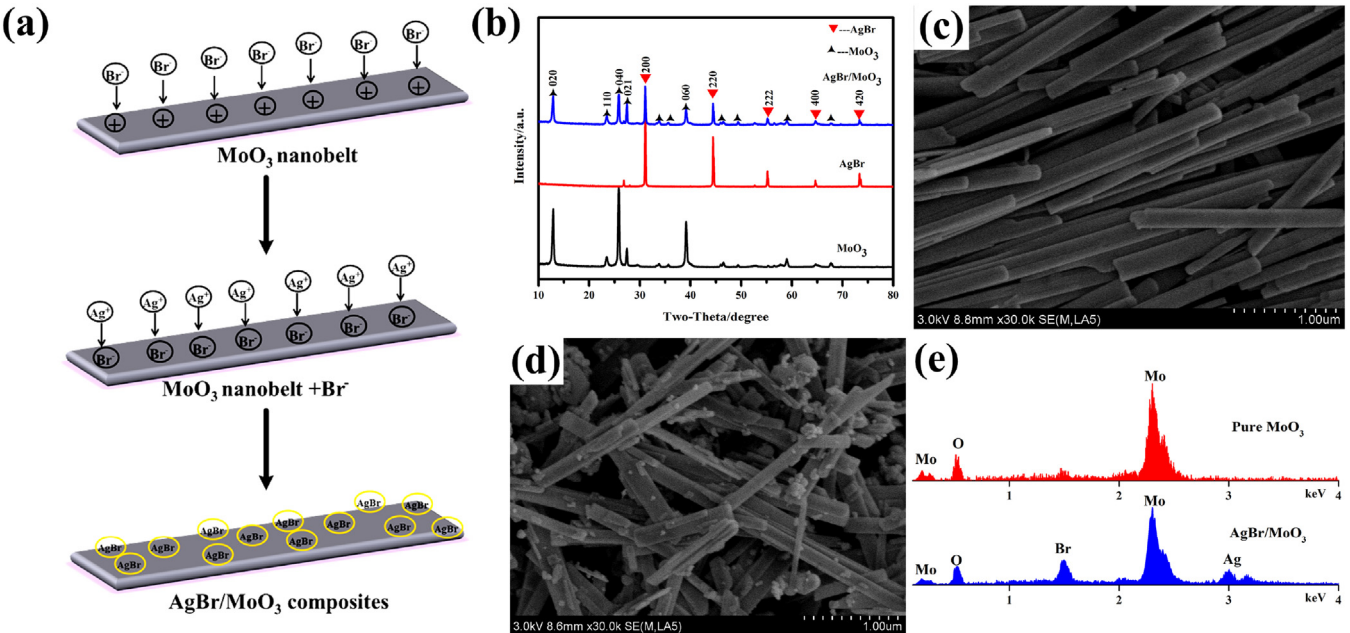


**Fig. 1.** a) Schematic illustration of preparation process of the AgBr/MoO<sub>3</sub> nanocomposite. b) XRD patterns of the as-prepared MoO<sub>3</sub>, AgBr, and AgBr/MoO<sub>3</sub>. c) FESEM images of c) MoO<sub>3</sub>, d) AgBr/MoO<sub>3</sub>. e) Corresponding EDS spectrum of MoO<sub>3</sub>, and AgBr/MoO<sub>3</sub>.

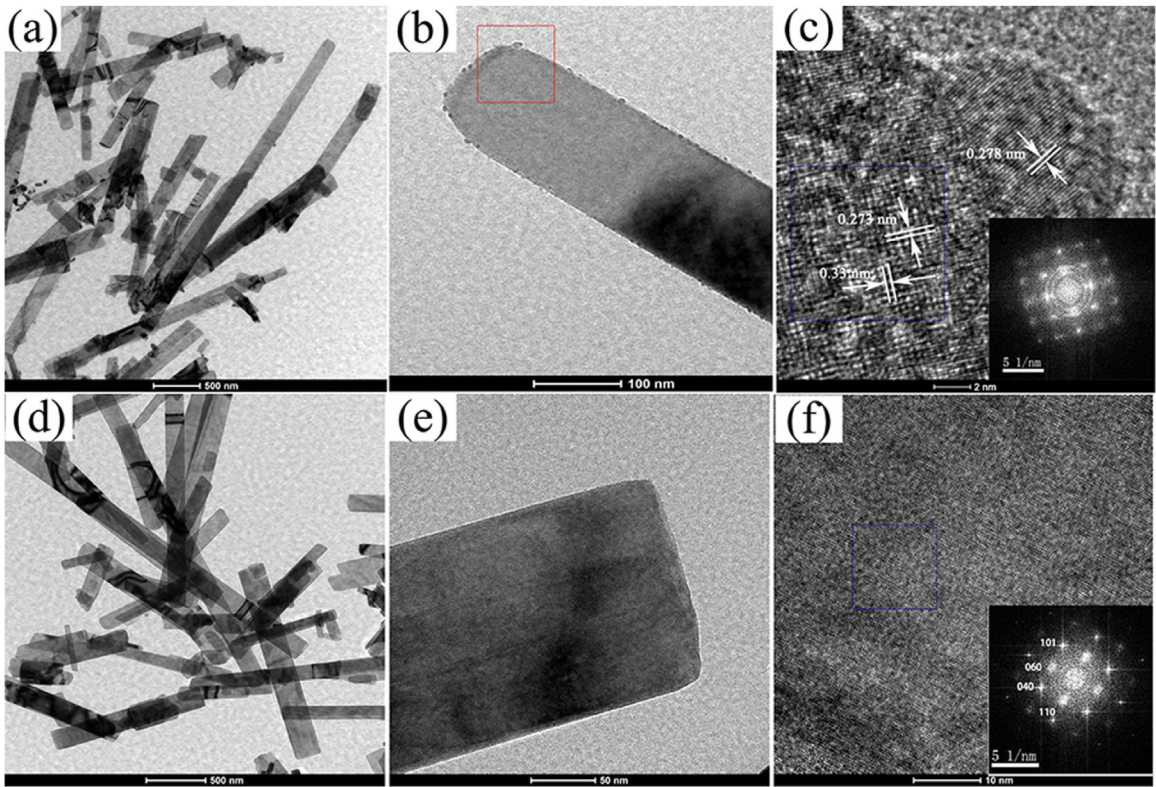


**Fig. 2.** a), b) low TEM images and c) HRTEM images of AgBr/MoO<sub>3</sub> nanocomposite; d), e) low TEM images and f) HRTEM images of MoO<sub>3</sub> nanobelts.

ties were investigated in a homemade three-electrode cell by using a computer-controlled electrochemical workstation. Briefly, AgBr/MoO<sub>3</sub> composites (100 mg) were suspended in absolute ethyl alcohol solution (10 mL) and the suspension were ultrasonically scattered to form a homogeneous solution. Fluorine doped stannic oxide (FTO) electrode was cleaned with NaOH (1 mol L<sup>-1</sup>) and H<sub>2</sub>O<sub>2</sub> (30 wt%), washed with acetone and deionized water, then dried at room temperature. Then, 0.1 mL of the above solution was

dropped onto the FTO glass with fixed area (1 cm<sup>2</sup>). After evaporation in an ambient environment, the FTO glasses with catalysts were put into the bake oven (70 °C) overnight, and then the catalysts were found attached tightly onto the surface of FTO glass. The prepared pure MoO<sub>3</sub>@FTO or AgBr/MoO<sub>3</sub>@FTO, a platinum sheet, and a mercurous chloride electrode were employed as working electrode, counter electrode, and reference electrode respectively, and 2 mol L<sup>-1</sup> Na<sub>2</sub>SO<sub>4</sub> was used as the electrolyte.

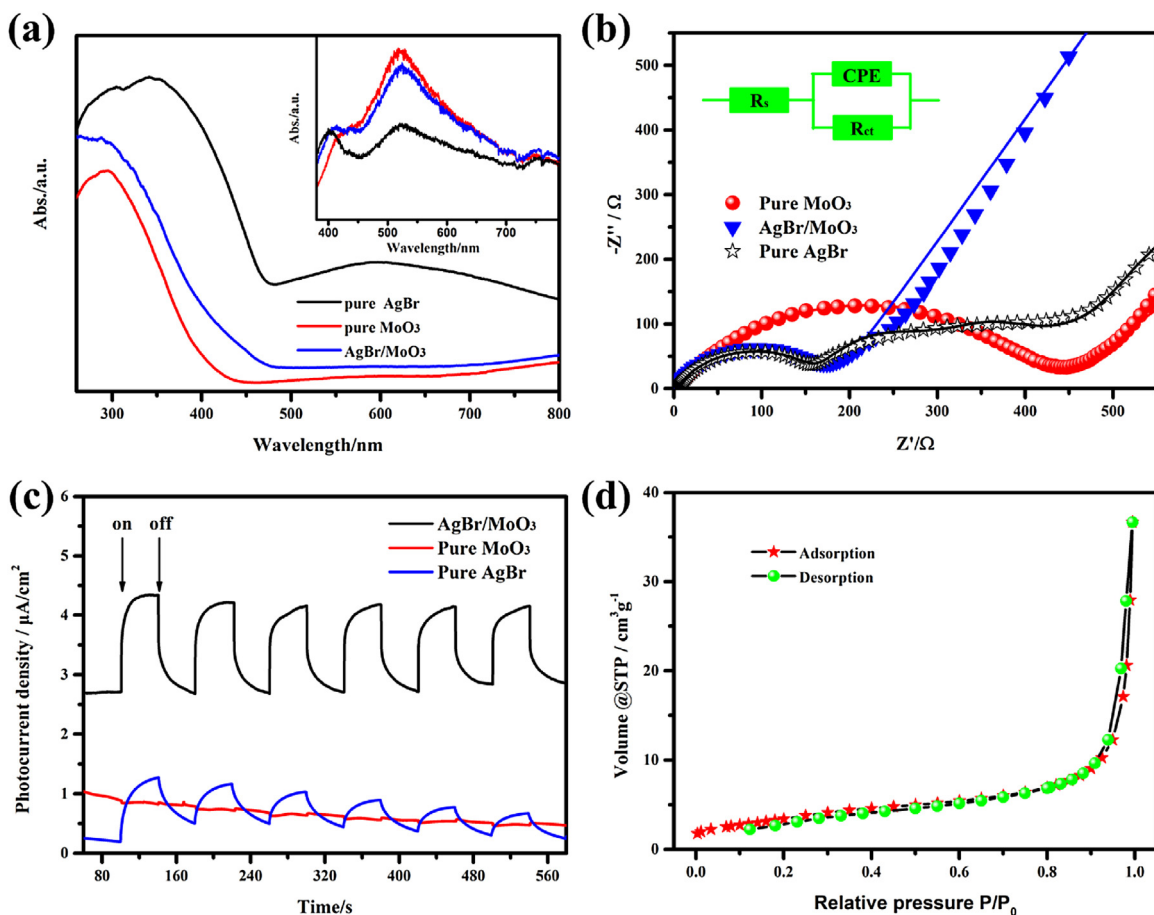


**Fig. 3.** a) UV-vis diffuse reflectance and PL (inset) spectra of pure MoO<sub>3</sub>, pure AgBr and AgBr/MoO<sub>3</sub> nanocomposite. b) Electrochemical impedance spectroscopy Nyquist plots of MoO<sub>3</sub>, AgBr and AgBr/MoO<sub>3</sub> nanocomposite. The solid line was fitted by ZSimpWin software using the proposed equivalent circuit model. The inset shows an ideal equivalent circuit for the working photoelectrode. c) Time-dependent photocurrent density of MoO<sub>3</sub>, AgBr and AgBr/MoO<sub>3</sub> nanocomposite. d) N<sub>2</sub> adsorption-desorption isotherm of AgBr/MoO<sub>3</sub>.

#### 2.4. Photocatalytic activity

In most reported research, Rhodamine B (RhB) is commonly used in organic dye pollutants. Visible-light-driven photocatalytic activity of the as-prepared samples was evaluated by degradation of RhB under a 250 W Xenon lamp irradiation at room temperature. In a typical photocatalytic experiment process, 200 mL RhB (10 mg L<sup>-1</sup>) and 0.04 g of each catalyst were added into the photocatalytic reaction device. The mixture was magnetically stirred in the dark for 1 h to attain absorption–desorption equilibrium between the RhB and surface of photocatalyst before irradiation. At regular interval times, about 5 mL of suspensions were collected and separated by centrifuge (8000 rpm, 2 min) two times to remove the photocatalyst particles. The removal of RhB during the photodegradation process was monitored based on the absorption at 554 nm by using a UV-vis spectrophotometer. And then the absorption value was transformed to concentration by using the standard curve of RhB.

#### 2.5. Theoretical calculations

Plane-wave-density function (DFT) calculation for MoO<sub>3</sub>, AgBr, AgBr/MoO<sub>3</sub> were performed using Dmol 3 program (Materials Studio, Accelrys Inc.). Perdew–Burke–Ernzerh (PBE) of generalized gradient approximation (GGA) was used as the exchange–correlation function in this work. SFC tolerance for AgBr, MoO<sub>3</sub>, and AgBr/MoO<sub>3</sub> were  $1 \times 10^{-5}$  eV per atom. Monkhorst-Pack point sets of  $2 \times 2 \times 2$ ,  $4 \times 1 \times 4$ , and  $1 \times 1 \times 3$  were used

for AgBr, MoO<sub>3</sub> and AgBr/MoO<sub>3</sub> respectively. Smearing value for AgBr and MoO<sub>3</sub> were 0.005 Ha, and it is 0.05 Ha for AgBr/MoO<sub>3</sub>. Pseudo-atomic calculations were performed for the O 2s<sup>2</sup>2p<sup>4</sup>, Mo 4s<sup>2</sup>4p<sup>6</sup>4d<sup>5</sup>5s<sup>1</sup>, Ag 5s<sup>1</sup>, and Br 4s<sup>2</sup>4p<sup>5</sup> states of the valence electrons.

### 3. Results and discussions

#### 3.1. Formation and characterization of AgBr/MoO<sub>3</sub> nanobelts composite

The proposed formation of AgBr/MoO<sub>3</sub> nanocomposite was associated with the oriented diffusion of Br<sup>-</sup> and the subsequent reaction with Ag<sup>+</sup> on the MoO<sub>3</sub> nanobelts surface, as schematically described in Fig. 1a. When the MoO<sub>3</sub> nanobelts were homogeneously dispersed in ethanol solution at room temperature, introducing Br<sup>-</sup> ions into the solutions contributed to surface adsorption ascribed to the positive charges of the MoO<sub>3</sub> nanobelts surfaces. Once Ag<sup>+</sup> ions were injected, it would easily react with Br<sup>-</sup> ions and ultimately form AgBr/MoO<sub>3</sub> nanocomposite with the extension of mixing time. X-ray diffraction (XRD) patterns shown in Fig. 1b confirms the formation of the AgBr/MoO<sub>3</sub> nanocomposite juxtaposed with the obtained pure MoO<sub>3</sub> and AgBr. All the established peaks for the AgBr/MoO<sub>3</sub> nanocomposite with a mole ratio of 1:3 could be indexed to the orthorhombic  $\alpha$ -MoO<sub>3</sub> (JCPDS card no. 05-0508) and AgBr (JCPDS card no. 79-0149). The strong diffraction peaks of (020), (040), and (060) plane suggest that the obtained nanocomposite retained the anisotropic morphology

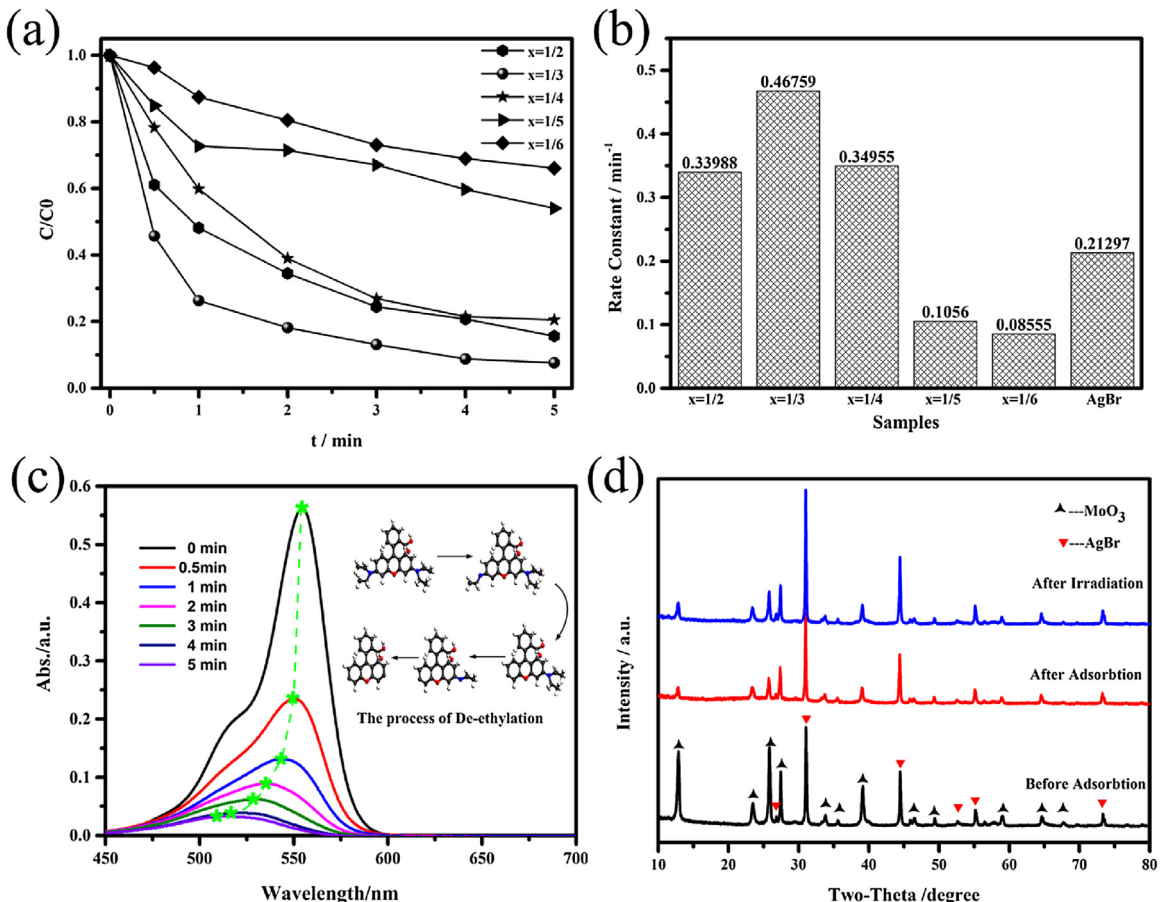


**Fig. 4.** a) Photocatalytic degradation of RhB in the presence of different contents of AgBr photocatalysts under visible-light irradiation. b) Comparison of apparent rate constants ( $k_{app}$ ) of the obtained photocatalysts for RhB degradation. c) Temporal absorption spectral changes of RhB and process of de-ethylated (inset) during the photodegradation process using AgBr/MoO<sub>3</sub> (1:3) nanocomposite. d) XRD patterns of AgBr/MoO<sub>3</sub> (1:3) before and after photocatalytic process.

with the (010) face of the MoO<sub>3</sub> [26]. The AgBr contents in the AgBr/MoO<sub>3</sub> nanocomposites modulated the intensity of the diffraction peaks (seen in Fig. S2), and  $I_{MoO_3}(021)/I_{AgBr}(200)$  decreased gradually with increasing AgBr:MoO<sub>3</sub> molar ratio. The morphology and composition of the AgBr/MoO<sub>3</sub> nanocomposite (1:3) was further investigated by FESEM and TEM characterizations. As seen in Figs. 1 d and 2 a and b, the nanocomposite displayed a distinct AgBr-loaded MoO<sub>3</sub> structure, which is different from the pure MoO<sub>3</sub> nanobelts (Figs. 1 c and 2 d and e), and the obtained composite was composed of the elements Mo, O, Ag and Br without any other impurities (Fig. 1 e). Besides some larger sizes of nanoparticles, other small AgBr nanoparticles less than 10 nm, which could not be seen from SEM image, were observed from TEM image (Fig. 2 b). The growth of these AgBr nanoparticles was suppressed in the formation process of the AgBr/MoO<sub>3</sub> nanocomposite attributable to the interaction between the Ag<sup>+</sup>/AgBr and the MoO<sub>3</sub> surface. In contrast, 1–3 μm size of AgBr particles could be obtained in alcoholic solution in absence of MoO<sub>3</sub> nanobelts (Fig. S3). From Fig. 2 c, the spacing with 0.278 nm of the adjacent lattice planes was consistent with the (200) crystal facet of AgBr [27], and the lattice fringes with lattice spacing of 0.330 nm and 0.273 nm correlate with the (040) and (101) plane of MoO<sub>3</sub>, respectively [28]. Concurrently, the ring-like SAED pattern for the surface of the AgBr/MoO<sub>3</sub> (the inset of Fig. 2 c) proved that the AgBr nanoparticles were distributed on the MoO<sub>3</sub> nanobelts in comparison with the spot pattern for pure MoO<sub>3</sub> (Fig. 2 d–f).

From UV-vis diffuse reflectance spectra (Fig. 3 a), the absorption edge of the AgBr/MoO<sub>3</sub> composite showed an obvious red-shift of ~40 nm while it is located at 430 nm for the pure MoO<sub>3</sub>; even

the absorption intensity of the composite is stronger than that of the MoO<sub>3</sub> nanobelts, indicating the improvement of absorption capacity by loading of the AgBr nanoparticles on the surfaces of the MoO<sub>3</sub> nanobelts due to the strong absorption of the AgBr [29]. Simultaneously, the PL intensity of the main emission peak located in ~525 nm slightly decreased for the AgBr/MoO<sub>3</sub> nanocomposite with comparison to that of the MoO<sub>3</sub>, as shown in the inset of Fig. 3 a. It maybe attribute to the recombination from CB of the MoO<sub>3</sub> to VB of the AgBr caused by formation of Z-scheme between the MoO<sub>3</sub> and the AgBr, while the emission peak of ~520 nm for the MoO<sub>3</sub> was designated to be the existence of oxygen vacancy defect sites on the surface [30]. Electrochemical Impedance Spectroscopy (EIS) [31–34] further evaluated kinetics of charge transfer of the obtained photocatalysis, as shown in Fig. 3 b. The Nyquist plot could be fitted according to the equivalent circuit (Randles–Ershler circuit model), and the arcs are related to charge transfer at interface of the semiconductor||electrolyte. The fitted value of  $R_{ct}$  was 183 Ω for the AgBr/MoO<sub>3</sub> composite, it is close to the pure AgBr (168 Ω) and about 2.3 times smaller than the pure MoO<sub>3</sub> nanobelts (415 Ω). Accordingly, the AgBr/MoO<sub>3</sub> composite had a preferable efficiency of charge transfer and reducing charge recombination efficiency. This could be entirely supported by photocurrent–time behaviors (shown in Fig. 3 c), which evaluated the interfacial separation and generation dynamics of photo-induced charges of the semiconductor photocatalysts. The photocurrent–time (I–t) characteristics revealed that the AgBr/MoO<sub>3</sub> composite electrode presented a periodic on/off response, and the responding photocurrent density is about 1.7 μA cm<sup>-2</sup>. However, weak photocurrent responses were observed for the pure MoO<sub>3</sub> nanobelts and the pure AgBr under

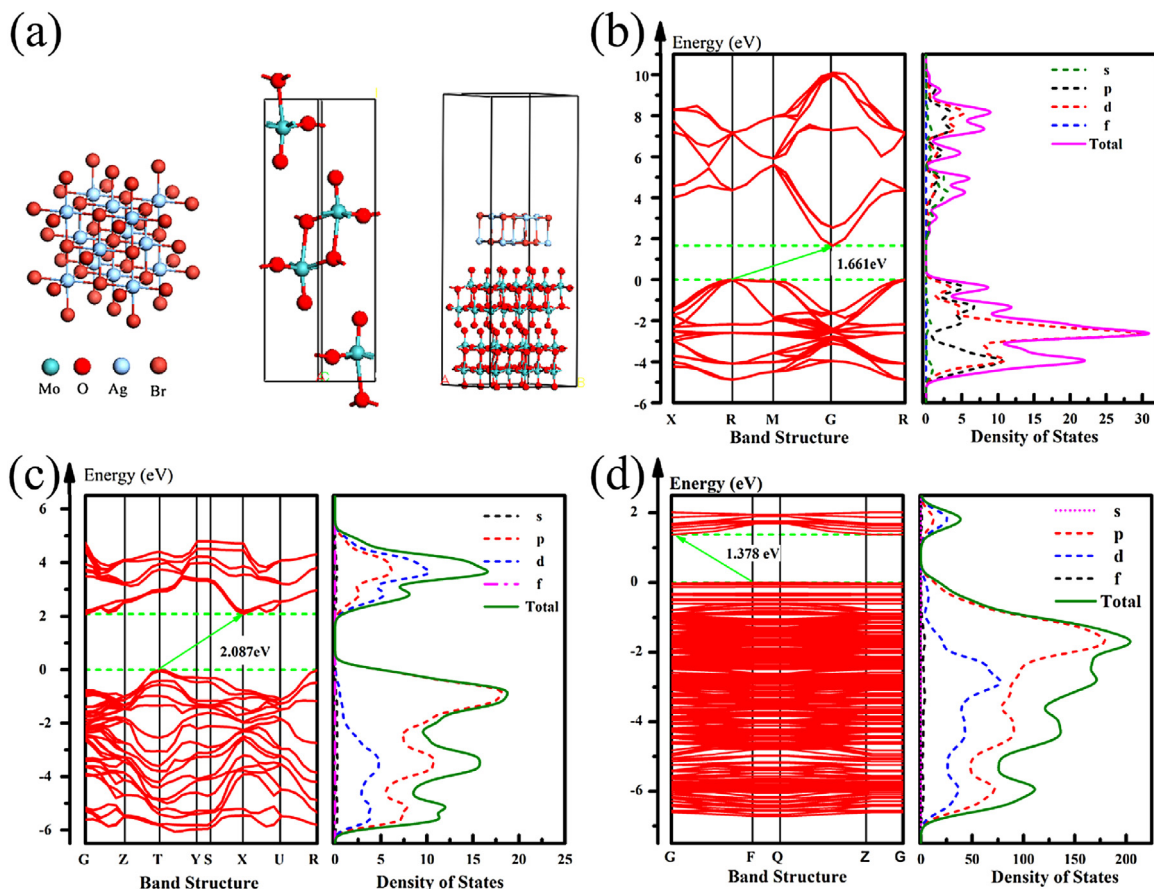


**Fig. 5.** a) Optimized geometric structures of AgBr, MoO<sub>3</sub> and AgBr/MoO<sub>3</sub> nanocomposite. Band structures and the density of state of b) AgBr, c) MoO<sub>3</sub> and d) AgBr/MoO<sub>3</sub> nanocomposite calculated through the density functional method.

the same on/off condition. Such results demonstrated that the AgBr/MoO<sub>3</sub> composite performed higher separation and transfer efficiency of the photo-induced charges under visible light irradiation. Surprisingly, the enhancing property of the AgBr/MoO<sub>3</sub> composite in the photocatalysis system was not attributed to its large surface area. This is because its BET surface area was  $\sim 13 \text{ m}^2 \text{ g}^{-1}$ , which is similar to that of the pure MoO<sub>3</sub> ( $\sim 14 \text{ m}^2 \text{ g}^{-1}$ ) and is larger than that of the pure AgBr ( $\sim 2 \text{ m}^2 \text{ g}^{-1}$ ), as shown in Fig. 3d and S4. Therefore, the significant photocatalytic character should be ascribed to the aforementioned AgBr/MoO<sub>3</sub> heterostructure formed by the crystal growth inhibition effect, and such composite will certainly exhibit great possibilities in the fields of water oxidation, pollutant degradation, photodetector, etc.

### 3.2. Photocatalytic performance of the AgBr/MoO<sub>3</sub> composites

The highly photocatalytic activities of the AgBr/MoO<sub>3</sub> composites were evaluated by the degradation of Rhodamine B (10 mg L<sup>-1</sup>) under visible-light irradiation for 5 min after adsorption equilibrium, as shown in Fig. 4a. The Ag/Mo ratio certainly has a distinct effect on the degradation rate. The AgBr/MoO<sub>3</sub> composite with Ag/Mo mole ratio of 1:3 reveals more superior photocatalytic degradation activity than the other samples, and its degradation efficiency reached 95%, attributing to the highest intuitionistic  $k_{app}$  value of 0.468 min<sup>-1</sup>, which is more than twice of the pure AgBr (0.213 min<sup>-1</sup>) (Fig. 4b and Fig. S5). According to a previous report [35], too much AgBr could narrow the space charge region, and light penetration depth for MoO<sub>3</sub> might surpass the space charge layer, resulting in easier recombination of the photon-generated carrier in semiconductors. Approximately, too little AgBr lessened the quantity of available electron and hole trapping carriers against

the photocatalytic activity. Consequently, the content of AgBr is extremely crucial to photocatalytic activity of the AgBr/MoO<sub>3</sub> composite.

In the process of photodegradation, we not only observed marked decreasing in intensity, but also the blue shift of the maximum absorption peak for the RhB (at 554 nm) with increasing irradiation time (Fig. 4c). Rapid decreasing in intensity occurring with the fading of the RhB suggested valid decomposition within 5 min, and the blue shift for the absorption peak was attributed to the reaction of de-ethylated in the irradiating process [36], as depicted in the inset of Fig. 4c. Simultaneously, the photocurrent-time (I-t) of 5 min irradiation (shown in Fig. S6) demonstrated that the responding photocurrent density was not receded discernibly, which corresponds to the degradation curve in Fig. 4c and further proves the ultra-fast degradation rate. Through the special decomposing process, in spite of various initial concentration of pollutant (10–20 g L<sup>-1</sup>), the AgBr/MoO<sub>3</sub> (1:3) composite perseveringly maintained high efficiency above 80% (Fig. S7), and even the decomposition rate remained high (89.4%) after reuse (Fig. S8), offering the potential for practical applications. Correspondingly, XRD technique tested the phase structure of the AgBr/MoO<sub>3</sub> composite before and after dark adsorption and photocatalytic experiments (Fig. 4d), and the specific diffractive peaks of the sample did not change after reaction, which further demonstrates the significant stability of such a novel photocatalyst.

### 3.3. Density functional theory calculations of AgBr/MoO<sub>3</sub> structures

Density functional theory (DFT) was applied to calculate electronic structure of the AgBr/MoO<sub>3</sub> heterostructure composite

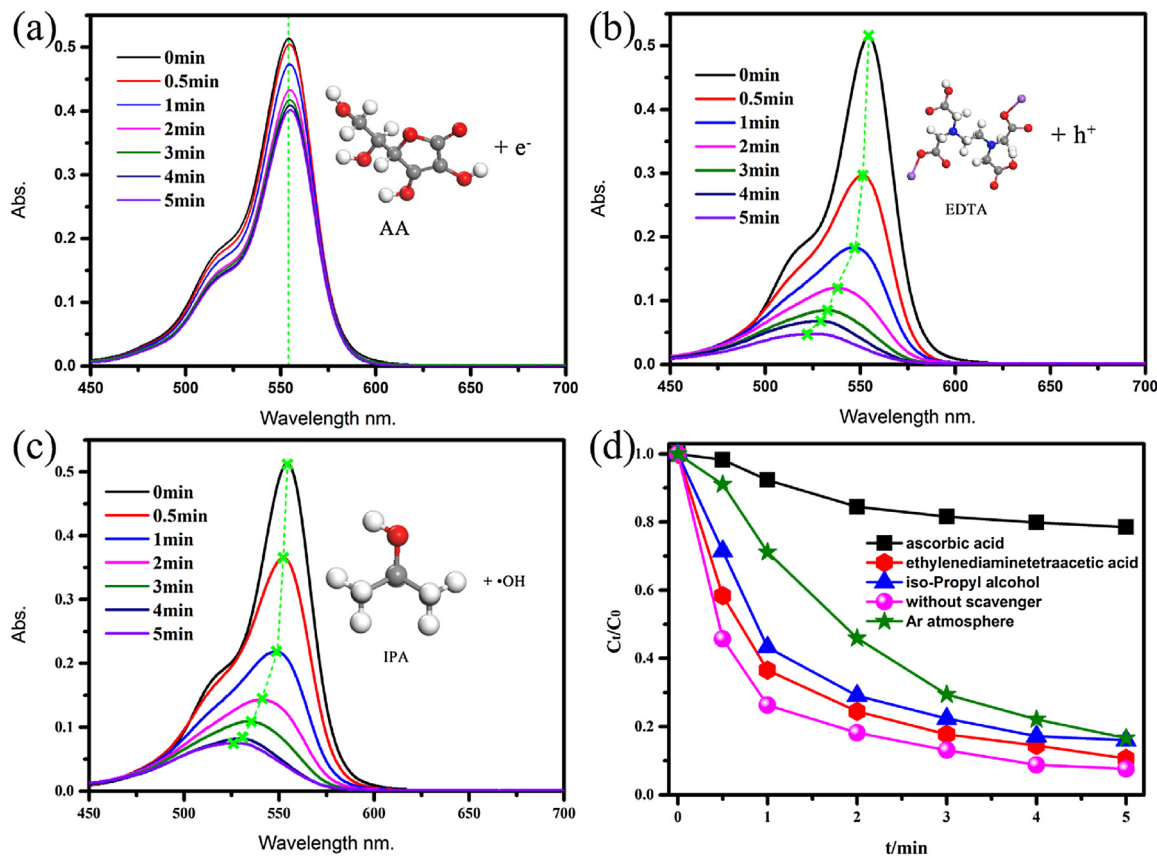


**Fig. 6.** Temporal absorption spectral changes of RhB during the trapping experiments by using a) AA, b) EDTA, and c) IPA, d) Photocatalytic degradation curves of RhB solution under visible-light irradiation in the control experiments.

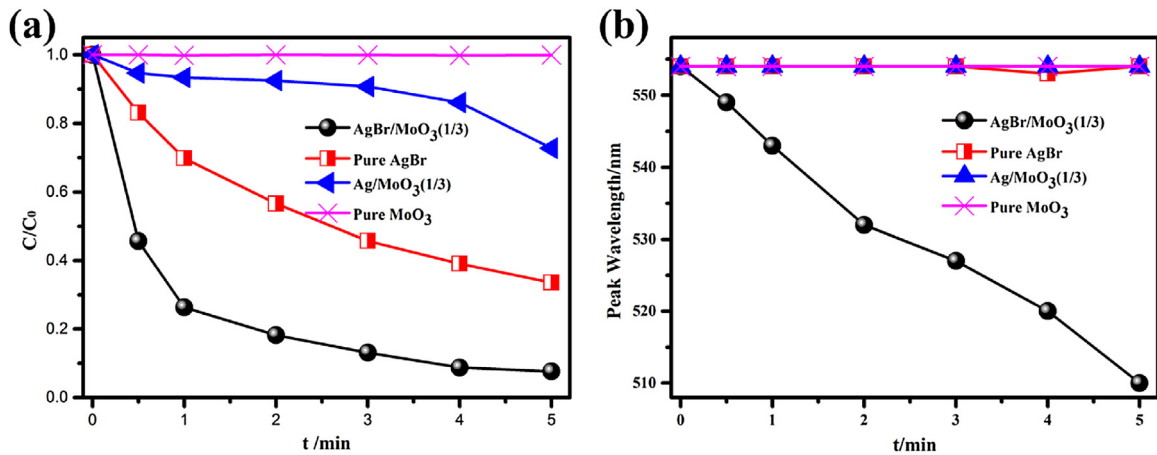


**Fig. 7.** a) Photocatalytic degradation of RhB in the presence of different photocatalysts under visible-light irradiation. b) Temporal absorption peak wavelength of RhB by different photocatalysts as a function of irradiation time.

because it significantly influences the efficiency of photocatalyst in the conduction band and valence band levels [37]. The building initial unit cells verified by XRD and HRTEM, AgBr (space group No. 225; Fm-3m), MoO<sub>3</sub> (space group No. 62; Pbnm) and AgBr(200)/MoO<sub>3</sub>(010) unit cell are shown in Fig. 5a, respectively. The calculated band gap of the AgBr/MoO<sub>3</sub> composite is 1.378 eV, which is much smaller than those of the pure AgBr (1.661 eV) and MoO<sub>3</sub> (2.087 eV). Also, the highly dispersive valence band (VB<sub>MAX</sub> being located at R point) and conduction band (CB<sub>MIN</sub> being located at G point) for the AgBr was conducive to the transport of the excited charge carriers, which is important for high photocatalytic activ-

ity. It should be noted that the underestimated band gaps, which were smaller than the corresponding experimental values (Fig. 5b and c), were attributed to the inherent defect of DFT methods [38,39]. According to the UV-vis diffuse reflectance spectroscopy, the changing trend of the band gaps in the theoretical calculations is consistent with the experimental results. The relevant total density of state (TDOS) and the project density of state (PDOS) revealed orbital states of electrons in the AgBr/MoO<sub>3</sub> composite, as shown in Fig. 5d. VBs were occupied by O 2p and Br 4P orbital, whereas the CBs were composed of Mo 4d orbitals, which is different from those of the AgBr (VBs: Ag 4d and Br 4P; CBs: Ag 5s and Br 3d) and

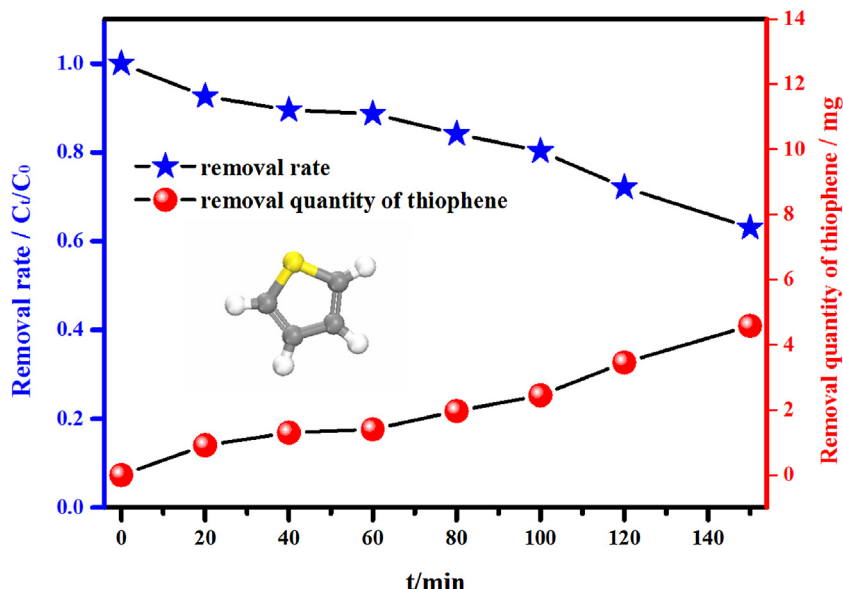


**Fig. 8.** Photocatalytic degradation curves of thiophene solution and its corresponding degradation amount.

the MoO<sub>3</sub> (VBs: O 2p; CBs: Mo 4d and a little from O 2p) (Fig. 5b and c). As a result, VBM of the AgBr/MoO<sub>3</sub> has been upshifted, caused by the hybridization between the Br 4p orbital and the O 2p orbital leading towards the narrow band gap.

#### 3.4. Visible-light-driven photocatalytic mechanism of the AgBr/MoO<sub>3</sub> catalyst

Under visible-light irradiation, a large amount of reactive species, such as photogenerated •O<sub>2</sub><sup>-</sup>, h<sup>+</sup> and •OH, usually play a part in degradation of organic dyes [40]. To discover which specific species is dominant during the photodegradation process of RhB within a short period of time by using the AgBr/MoO<sub>3</sub> composite, several trapping experiments of the reactive oxygen species were carried out. (1) When ascorbic acid (AA) was used to inhibit the generation of superoxide radical (•O<sub>2</sub><sup>-</sup>) (Fig. 6a), the intensity of the absorption peak at 550 nm slowly decreased with irradiation time. (2) Ethylenediamine tetraacetic acid disodium salt (EDTA) was employed as the holes (h<sup>+</sup>) radical scavenger (Fig. 6b), and the intensity greatly decreased with irradiation time; additionally, the position of the strongest absorption peak even occurred obvious blue-shift. (3) 2-propanol (IPA) was employed as the hydroxyl radical (•OH) scavenger (Fig. 6c), and the changes of both the intensity and peak position were similar to (2). The corresponding curve of the degradation rate was shown in Fig. 6d, and the dramatically decreasing degradation rate with the 0.1 mmol AA addition implies that •O<sub>2</sub><sup>-</sup> played much more important role than •OH and h<sup>+</sup> in the photocatalytic process. (4) The degradation rate of RhB decreased clearly when Ar was bubbled, as shown in Fig. 6d and Fig. S9. It confirmed that the dissolved oxygen acted as an efficient electrons scavenger, resulting in the formation of the •O<sub>2</sub><sup>-</sup>. The role of the •O<sub>2</sub><sup>-</sup> could also be confirmed by further designed experiments. Fig. 7a showed the degradation curves of the obtained Ag/MoO<sub>3</sub>, pure AgBr, and MoO<sub>3</sub>, and the 25% degradation rate of the Ag/MoO<sub>3</sub> had only a certain enhancement compared with the pure MoO<sub>3</sub> attributable to the surface plasmon resonance (SPR) of Ag NP [41–43]. Wavelength curves of the corresponding maximum absorption peaks for the residual RhB solution during photocatalysis (Fig. 7b) revealed no apparent peak shift was observed in the presence of the Ag/MoO<sub>3</sub>, pure AgBr, or MoO<sub>3</sub>. Whereas the absorption peak shifts to ~510 nm after 5 min

irradiation for the AgBr/MoO<sub>3</sub>, implying the special de-ethylated reaction mechanism for •O<sub>2</sub><sup>-</sup> species in the photocatalytic process.

To ascertain whether the reactive electrons were donated from either photo-excited RhB dye molecules, photo-generation of electron in the CB of AgBr, or both under visible light irradiation. We conducted the AgBr/MoO<sub>3</sub> composites for decomposing colourless organic pollutants thiophene, and the degradation detail was described in SI. Fig. 8 showed that about 37% (5.18 mg) of thiophene was degraded in 150 min, indicating the photocatalytic activity of the AgBr/MoO<sub>3</sub> composites without dye sensitization effect. That is, the photogenerated electrons in the CB of AgBr played a crucial role in the degradation process of the thiophene. Therefore, the ultrafast degradation of the RhB on the AgBr/MoO<sub>3</sub> nanocomposites could be due to both the photocatalytic process and the dye sensitization.

The poor visible light degradation of the wide-bandgap MoO<sub>3</sub> suggested there must be a synergistic effect between the MoO<sub>3</sub> nanobelts and the AgBr quantum dots, which is responsible for the unexceptionable photocatalytic capacity of the AgBr/MoO<sub>3</sub> composite. The MoO<sub>3</sub> nanobelts possess a well adsorption capacity for the RhB, and the AgBr is very sensitive to the visible light. Thus, it is crucial and necessary to understand the enhancement of photocatalytic efficiency in a short period of time, as well as the elaborate in charge transfer process. Under the visible irradiation, the AgBr can be much more easily excited than the MoO<sub>3</sub>, and generate a lot of photoexcited electrons and holes. According to Kubelka-Munk bandgap estimation theory [9,44,45], the calculated conduction band of the AgBr (-0.07 eV) is higher than that of the MoO<sub>3</sub> (+0.34 eV), and the valence band is just the opposite (Fig. S10). Fermi levels of AgBr (-5.6 eV) and MoO<sub>3</sub> (-5.3 eV) tend to equal after forming AgBr/MoO<sub>3</sub> composite due to their different work functions [32,46]. In this process, the Fermi level of MoO<sub>3</sub> was maintained its position due to the Pinning effect of wide-band semiconductor while the Fermi level of AgBr could shift up until reaching equilibrium, then the Ohmic contact was formed in the contact surface as shown in Fig. 9. At the same time, the CB of AgBr moved to -0.37 eV vs. NHE and the VB was +2.38 eV vs. NHE. It is well known that many defects can be easily generated at the solid–solid contact interface. The Ohmic contact surface of the AgBr/MoO<sub>3</sub> serves as the center of photoinduced electron-hole recombination which will enhance the photocatalytic efficiency to some extent.

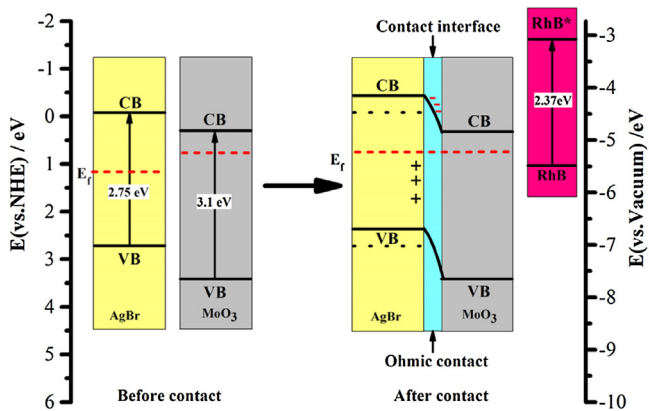


**Fig. 9.** Schematic illustration of photosensitized degradation of the RhB dyes over the AgBr/MoO<sub>3</sub> composite before and after contact.

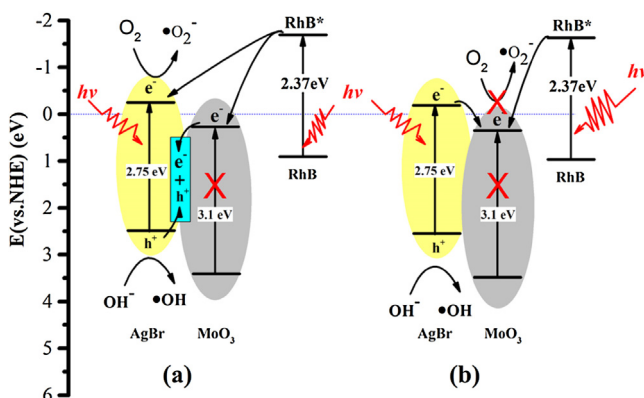


**Fig. 10.** Novel Z-scheme (a), and Heterojunction-type (b) charge-transfer mechanisms for the AgBr/MoO<sub>3</sub> system.

The possible separation process of the photon-generated carrier is described in Fig. 10a based on the above analysis. Once visible-light is irradiated, the photo-induced electrons quickly transferred from the excited RhB to the CB of MoO<sub>3</sub> via self-sensitization process of the dye; the accumulated electrons then immediately recombined with the photo-induced holes in the VB of AgBr in the Ohmic contact surface, leading to the accumulated rich electrons in the CB of AgBr and a small quantity of holes in the VB of AgBr. Favorably, the photo-induced electrons in the CB of AgBr can reduce the O<sub>2</sub> in the solution to •O<sub>2</sub><sup>-</sup> caused by the more negative E<sub>BCB</sub> (-0.37 eV vs. NHE) than the redox potential of O<sub>2</sub>/•O<sub>2</sub><sup>-</sup> (-0.33 eV vs. NHE) [47]. Moreover, the E<sub>TVB</sub> of the AgBr (+2.38 eV vs. NHE) is more positive than the redox potential of •OH/OH<sup>-</sup> (+1.99 eV vs. NHE), suggesting that the contribution of the small quantity of photo-induced holes in the VB of the AgBr is not insignificant. Therefore, this high photocatalytic activity of the AgBr/MoO<sub>3</sub> heterojunction materials is attributed to the high separation and easy transfer of the photogenerated carriers at the heterostructure interfaces, which consists of the suitable band positions between AgBr and MoO<sub>3</sub>. Remarkably, the recombination of Fermi level effect facilitated the injection of electrons in the dye-sensitized process and the superior adsorption capacity of MoO<sub>3</sub> nanobelts were also contributed to the higher photocatalytic efficiency. The proposed separation process was well agreed with the results of our experiments. Differently, if the photo-induced electrons in the CB of AgBr could easily migrate to the CB of MoO<sub>3</sub>, and the photogenerated holes remain in the VB of AgBr (Fig. 10b), the photo-induced electrons in the CB of MoO<sub>3</sub> cannot reduce O<sub>2</sub> into •O<sub>2</sub><sup>-</sup> with the

redox potential of -0.33 eV vs. NHE, attributable to the positive E<sub>BCB</sub> (+0.34 eV vs. NHE).

#### 4. Conclusions

In summary, a composite photocatalytic system of AgBr quantum dots interspersed MoO<sub>3</sub> nanobelts has been successfully constructed through a simple and handy way, and the composite displayed high degradation efficiency of 95% for Rhodamine B solution under visible-light irradiation within 5 min. Theoretical calculations indicated that the changing trend of the band gaps is consistent with the experimental results. Further experiments suggested that •O<sub>2</sub><sup>-</sup> played a much more important role than •OH and h<sup>+</sup> in the photocatalytic process, and degradation of the RhB on the AgBr/MoO<sub>3</sub> nanocomposite was due to both the photocatalytic process and the dye sensitization. Mechanism analysis showed that the formation of well-defined novel Z-scheme between AgBr and MoO<sub>3</sub> effectively facilitates dye-sensitization and charge transfer, resulting in high activity in degrading RhB solution under visible-light irradiation. These results developed the potential use of an effective composite material to prompt the photosensitization process of dye, and opened up new insights into surface- and interface-engineering techniques, enhancing the photocatalytic degradation efficiency and further utilization in the field of environmental improvement or energy transformation.

#### Acknowledgements

The work is supported by Jiangsu postdoctoral scientific research fund (1202016C), the National Nature Science Foundation of China (NSFC No. 51372114), Natural Science Foundation (NSF) of Jiangsu Province (BK20151198), the Open Project of Jiangsu Key Laboratory for Environment Functional Materials (SJHG1310) and A Project Funded by the Priority Academic Program Development of Jiangsu Higher Education Institutions(PAPD).

#### Appendix A. Supplementary data

Supplementary data associated with this article can be found, in the online version, at <http://dx.doi.org/10.1016/j.apcatb.2017.01.029>.

#### References

- [1] H. Leng, J. Loy, V. Amin, E.A. Weiss, M. Pelton, ACS Energy Lett. 1 (2016) 9–15.
- [2] J. Ding, Y. Bu, M. Ou, Y. Yu, Q. Zhong, M. Fan, Appl. Catal. B: Environ. 202 (2017) 314–325.
- [3] D. Deng, K.S. Novoselov, Q. Fu, N. Zheng, Z. Tian, X. Bao, Nat. Nanotechnol. 11 (2016) 218–230.
- [4] L. Zhang, Y. Zhu, Catal. Sci. Technol. 2 (2012) 694.
- [5] J. Jiang, K. Zhao, X. Xiao, L. Zhang, J. Am. Chem. Soc. 134 (2012) 4473–4476.
- [6] H. Tong, S. Ouyang, Y. Bi, N. Umezawa, M. Oshikiri, J. Ye, Adv. Mater. 24 (2012) 229–251.
- [7] S. Thaweesak, M. Lyu, P. Peerakiatkajohn, T. Butburee, B. Luo, H. Chen, L. Wang, Appl. Catal. B: Environ. 202 (2017) 184–190.
- [8] H. Xu, J. Yan, Y. Xu, Y. Song, H. Li, J. Xia, C. Huang, H. Wan, Appl. Catal. B: Environ. 129 (2013) 182–193.
- [9] W. Wang, X. Huang, S. Wu, Y. Zhou, L. Wang, H. Shi, Y. Liang, B. Zou, Appl. Catal. B: Environ. 134–135 (2013) 293–301.
- [10] D. Jiang, L. Chen, J. Zhu, M. Chen, W. Shi, J. Xie, Dalton Trans. 42 (2013) 15726–15734.
- [11] E.N.K. Glover, S.G. Ellington, G. Sankar, R.G. Palgrave, J. Mater. Chem. A 4 (2016) 6946–6954.
- [12] J. Yan, H. Wu, H. Chen, Y. Zhang, F. Zhang, S.F. Liu, Appl. Catal. B: Environ. 191 (2016) 130–137.
- [13] Z. Pan, T. Hisatomi, Q. Wang, M. Nakabayashi, N. Shibata, C. Pan, T. Takata, K. Domen, Appl. Catal. A: Gen 521 (2016) 26–33.
- [14] H. Li, T. Hu, R. Zhang, J. Liu, W. Hou, Appl. Catal. B: Environ. 188 (2016) 313–323.
- [15] W. Li, C. Feng, S. Dai, J. Yue, F. Hua, H. Hou, Appl. Catal. B: Environ. 168–169 (2015) 465–471.
- [16] T. Liu, B. Li, Y. Hao, Z. Yao, Chem. Eng. J. 244 (2014) 382–390.

- [17] X. Cao, B. Zheng, W. Shi, J. Yang, Z. Fan, Z. Luo, X. Rui, B. Chen, Q. Yan, H. Zhang, *Adv. Mater.* 27 (2015) 4695–4701.
- [18] P.R. Brown, R.R. Lunt, N. Zhao, T.P. Osedach, D.D. Wanger, L.Y. Chang, M.G. Bawendi, V. Bulovic, *Nano Lett.* 11 (2011) 2955–2961.
- [19] S. Hariharan, K. Saravanan, P. Balaya, *Electrochem. Commun.* 31 (2013) 5–9.
- [20] Z. Chen, D. Cummins, B.N. Reinecke, E. Clark, M.K. Sunkara, T.F. Jaramillo, *Nano Lett.* 11 (2011) 4168–4175.
- [21] Y. Ma, Y. Jia, Z. Jiao, L. Wang, M. Yang, Y. Bi, Y. Qi, *Mater. Lett.* 157 (2015) 53–56.
- [22] S. Balendhran, S. Walia, H. Nili, J.Z. Ou, S. Zhuiykov, R.B. Kaner, S. Sriram, M. Bhaskaran, K. Kalantar-zadeh, *Adv. Funct. Mater.* 23 (2013) 3952–3970.
- [23] M. Lu, C. Shao, K. Wang, N. Lu, X. Zhang, P. Zhang, M. Zhang, X. Li, Y. Liu, *ACS Appl. Mater. Interfaces* 6 (2014) 9004–9012.
- [24] L. Huang, H. Xu, R. Zhang, X. Cheng, J. Xia, Y. Xu, H. Li, *Appl. Surf. Sci.* 283 (2013) 25–32.
- [25] G. Li, L. Jiang, S. Pang, H. Peng, Z. Zhang, *J. Phys. Chem. B* 110 (2006) 24472–24475.
- [26] K. Sakaushi, J. Thomas, S. Kaskel, J. Eckert, *Chem. Mater.* 25 (2013) 2557–2563.
- [27] H. Li, S. Gan, H. Wang, D. Han, L. Niu, *Adv. Mater.* 27 (2015) 6906–6913.
- [28] Z. Shao, J. Jie, Z. Sun, F. Xia, Y. Wang, X. Zhang, K. Ding, S.T. Lee, *Nano Lett.* 15 (2015) 3590–3596.
- [29] J. Fu, B. Chang, Y. Tian, F. Xi, X. Dong, *J. Mater. Chem. A* 1 (2013) 3083.
- [30] L.X. Song, J. Xia, Z. Dang, J. Yang, L.B. Wang, J. Chen, *CrystEngComm.* 14 (2012) 2675–2682.
- [31] H. Li, Y. Sun, B. Cai, S. Gan, D. Han, L. Niu, T. Wu, *Appl. Catal. B: Environ.* 170–171 (2015) 206–214.
- [32] H. Huang, Y. He, X. Du, P.K. Chu, Y. Zhang, *ACS Sustain. Chem. Eng.* 3 (2015) 3262–3273.
- [33] M. Ge, C. Cao, S. Li, S. Zhang, S. Deng, J. Huang, Q. Li, K. Zhang, S.S. Al-Deyab, Y. Lai, *Nanoscale* 7 (2015) 11552–11560.
- [34] C. Han, Z. Chen, N. Zhang, J.C. Colmenares, Y.-J. Xu, *Adv. Funct. Mater.* 25 (2015) 221–229.
- [35] H. Xu, Y. Xu, H. Li, J. Xia, J. Xiong, S. Yin, C. Huang, H. Wan, *Dalton Trans.* 41 (2012) 3387–3394.
- [36] C. Chen, W. Ma, J. Zhao, *Chem. Soc. Rev.* 39 (2010) 4206–4219.
- [37] S. Ouyang, J. Ye, *J. Am. Chem. Soc.* 133 (2011) 7757–7763.
- [38] M. Long, P. Hu, H. Wu, Y. Chen, B. Tan, W. Cai, *J. Mater. Chem. A* 3 (2015) 5592–5598.
- [39] Z. Ma, Z. Yi, J. Sun, K. Wu, *J. Phys. Chem. C* 116 (2012) 25074–25080.
- [40] B. Tian, R. Dong, J. Zhang, S. Bao, F. Yang, J. Zhang, *Appl. Catal. B: Environ.* 158–159 (2014) 76–84.
- [41] X.H. Li, M. Antonietti, *Chem. Soc. Rev.* 42 (2013) 6593–6604.
- [42] L. Kuai, B. Geng, X. Chen, Y. Zhao, Y. Luo, *Langmuir* 26 (2010) 18723–18727.
- [43] S. Linic, P. Christopher, D.B. Ingram, *Nat. Mater.* 10 (2011) 911–921.
- [44] S. Yang, Y. Gong, J. Zhang, L. Zhan, L. Ma, Z. Fang, R. Vajtai, X. Wang, P.M. Ajayan, *Adv. Mater.* 25 (2013) 2452–2456.
- [45] X. Yang, H. Cui, Y. Li, J. Qin, R. Zhang, H. Tang, *ACS Catal.* 3 (2013) 363–369.
- [46] H. Yu, S. Chen, X. Quan, H. Zhao, Y. Zhang, *Appl. Catal. B: Environ.* 90 (2009) 242–248.
- [47] P. Zhou, J. Yu, M. Jaroniec, *Adv. Mater.* 26 (2014) 4920–4935.